



Published in final edited form as:

Bone. 2018 March ; 108: 71–78. doi:10.1016/j.bone.2017.12.023.

## Accuracy of MRI-based finite element assessment of distal tibia compared to mechanical testing

Chamith S. Rajapakse<sup>1,2</sup>, Elizabeth A. Kobe<sup>1</sup>, Alexandra S. Batzdorf<sup>1</sup>, Michael W. Hast<sup>2</sup>, and Felix W. Wehrli<sup>1</sup>

<sup>1</sup>Department of Radiology, University of Pennsylvania

<sup>2</sup>Department of Orthopaedic Surgery, University of Pennsylvania

### Abstract

High-resolution MRI-derived finite element analysis (FEA) has been used in translational research to estimate the mechanical competence of human bone. However, this method has yet to be validated adequately under *in vivo* imaging spatial resolution or signal-to-noise conditions. We therefore compared MRI-based metrics of bone strength to those obtained from direct, mechanical testing. The study was conducted on tibiae from 17 human donors (12 males and five females, aged 33 to 88 years) with no medical history of conditions affecting bone mineral homeostasis. A 25 mm segment from each distal tibia underwent MR imaging in a clinical 3-Tesla scanner using a fast large-angle spin-echo (FLASE) sequence at 0.137 mm × 0.137 mm × 0.410 mm voxel size, in accordance with *in vivo* scanning protocol. The resulting high-resolution MR images were processed and used to generate bone volume fraction maps, which served as input for the micro-level FEA model. Simulated compression was applied to compute stiffness, yield strength, ultimate strength, modulus of resilience, and toughness, which were then compared to metrics obtained from mechanical testing. Moderate to strong positive correlations were found between computationally and experimentally derived values of stiffness ( $R^2 = 0.77$ ,  $p < 0.0001$ ), yield strength ( $R^2 = 0.38$ ,  $p = 0.0082$ ), ultimate strength ( $R^2 = 0.40$ ,  $p = 0.0067$ ), and resilience ( $R^2 = 0.46$ ,  $p = 0.0026$ ), but only a weak, albeit significant, correlation was found for toughness ( $R^2 = 0.26$ ,  $p = 0.036$ ). Furthermore, experimentally derived yield strength and ultimate strength were moderately correlated with MRI-derived stiffness ( $R^2 = 0.48$ ,  $p = 0.0022$  and  $R^2 = 0.58$ ,  $p = 0.0004$ , respectively). These results suggest that high-resolution MRI-based finite element (FE) models are effective in assessing mechanical parameters of distal skeletal extremities.

### Keywords

MRI; Finite Element Analysis; Distal Tibia; Mechanical Testing

## Introduction

Impaired mechanical integrity of bone is a key manifestation of osteoporosis, predisposing millions of people to increased fracture risk. Fortunately, osteoporotic fracture risk can be alleviated through medication, adequate nutrition, and physical activity [1]. In order to manage osteoporosis properly, it is necessary to assess a patient's bone strength and associated risk of fracture.

Among those with osteoporosis, bone fracture risk is typically determined by bone mineral density (BMD), as measured by dual-energy X-ray absorptiometry (DXA) at the spine or proximal femur [2, 3]. However, BMD often fails to predict fracture risk accurately [4–9] and is unable to detect slight changes in bone structure over short periods of time [10]. An alternative method is the computer-based algorithm FRAX, which is capable of predicting fracture probability from some clinical risk factors, including age, sex, BMI, and use of glucocorticoids. However, FRAX does not take into account other important factors, such as secondary causes of osteoporosis, markers of bone turnover and bone mineral measurements at other sites, or explicit likelihood of falling, although this is indirectly built in through parameters such as age [11]. Because DXA-derived BMD measurements do not accurately track treatment efficacy over time or consider all factors necessary to predict fracture risk, alternative techniques capable of assessing bone mechanical properties are needed [12–14].

Due to its ability to resolve bone microstructure, high-resolution micro-computed tomography (micro-CT) is currently the preferred method for generating micro-level finite element (FE) models capable of evaluating bone mechanical competence [15]. Bone parameters derived from micro-CT FE analysis (FEA) have been shown to correlate with values obtained from direct, mechanical testing of trabecular bone specimens [16, 17]. Computer memory demands and the computational power needed to solve these FE models limit their feasibility for widespread clinical applications, although recent advances in nonlinear FE solvers have made it possible to perform these computationally intensive simulations on high-end desktop computers [18–21].

High-resolution peripheral quantitative computed tomography (HR-pQCT) and high-resolution magnetic resonance imaging (MRI) are two promising modalities for *in vivo* imaging of trabecular and cortical bone microarchitecture of the extremities. Images derived from these technologies have led to micro-FE models that are capable of estimating the mechanical competence of bone based on measures such as axial stiffness and failure strength [14, 21–25]. Furthermore, MRI and HR-pQCT possess the ability to monitor improvements in bone mechanical competence in response to treatment by tracking structural changes that are not detectable in BMD or bone volume fraction (BV/TV) over short time periods [26–29]. High-resolution MRI in particular possesses the potential for benefit, as it is able to image both appendicular [30, 31] and axial [32, 33] skeleton, as well as obtain complementary information—such as bone marrow composition [34, 35]—during the same scan session. However, compared to micro-CT, *in vivo* HR-pQCT and MRI resolutions are limited by radiation dose restrictions and the signal-to-noise ratio (SNR) imposed by scan time, respectively. Therefore, their accuracy in calculating mechanical properties must be assessed further [22].

To date, validation of high-resolution MRI-based FE model derived parameters has only been performed indirectly, via comparison to parameters obtained from micro-CT imaging of cadaveric bone [19, 22, 36]. Whole-bone axial stiffness of the distal tibia derived from high-resolution MRI FE models, which include both cortical and trabecular compartments, is strongly correlated with whole-bone stiffness obtained from high-resolution micro-CT images ( $R^2 = 0.85$ ) [19]. Furthermore, when the micro-CT FE models were downsampled to isotropic resolutions achievable by *in vivo* high-resolution MRI (100–160  $\mu\text{m}$ ), mechanical parameters were highly correlated ( $R^2 > 0.93$ ) with those obtained from micro-CT at resolutions before downsampling (25  $\mu\text{m}$ ) [19]. MacNeil and Boyd found HR-pQCT based nonlinear FE-derived apparent ultimate strength and experimentally determined strength of cadaveric distal radius samples to be highly correlated ( $R^2 = 0.96$ ;  $N = 5$ ) [37]. Additionally, Mueller *et al.* reported that HR-pQCT based FEA using an appropriately chosen failure strain criterion can estimate the experimentally determined strength of cadaveric human radius bones [23].

The objective of the present work was to directly validate MRI-based nonlinear measures of bone strength in the distal tibia by comparing them to results from mechanical testing of bone specimens derived from donors of a wide age range.

## Materials and Methods

### Specimens and Imaging

The human tibia specimens encompassing the distal metaphysis were extracted from 12 male and five female cadavers, aged 33 to 88 years, from the National Disease Research Interchange (NDRI). The specimens were harvested  $13.1 \pm 5.87$  hours post-mortem and stored for  $4.20 \pm 3.61$  years before being used. Donors with a medical history involving conditions affecting bone or bone mineral homeostasis were excluded. Specimens were then wrapped tightly in gauze and stored in airtight containers at  $-30^\circ\text{C}$  until further use.

A 25 mm thick segment, perpendicular to the bone's anatomic axis and including the distal metaphysis, was then sectioned (see analogous prior work [19]) from each tibia 15 mm proximal to the distal end plate using a reciprocating saw (Figure 1). This slab corresponded to the *in vivo* MRI scan region. Before imaging and mechanical testing, residual soft tissue on the periosteal cortex was removed carefully. The segments were then stored in the same manner as before sectioning.

The tibia specimens were imaged anterior side upward and distal end first, equivalent to the feet-first supine position in patient imaging of the ankle. All scanning was performed on a clinical 3T whole-body clinical MRI scanner (Siemens TIM Trio, Erlangen, Germany) using a 4-element receive-only surface coil (Insight MRI, Worcester, MA) previously used for MR imaging of the distal tibia in patients [38, 39]. Images were acquired with a 3D fast large-angle spin-echo (FLASE) pulse sequence with scan parameters matching those for patient imaging (flip angle  $140^\circ$ , repetition time/echo time 80/10.5 ms, field of view  $70 \times 53 \times 13 \text{ mm}^3$ , voxel size  $0.137 \times 0.137 \times 0.410 \text{ mm}^3$ ) with the third dimension corresponding to the axial direction requiring seven minute acquisition time [40]. Immediately after imaging, the specimens were stored at  $-30^\circ\text{C}$  until mechanical testing.

## Image processing

First, a filter algorithm was used to account for image inhomogeneity across the volume due to spatial sensitivity variations of the MR receive coil [41]. The resulting images were then processed to generate a 3D array known as a bone volume fraction (BVF) map, with each individual voxel value representing the fractional occupancy of bone (BV/TV) [42]. Grayscale pixel values were scaled linearly to cover the range from 0% to 100%, with pure marrow and pure bone having minimum and maximum values, respectively. These 3D arrays served as input to the FE model.

## Linear FE modeling

Each voxel in the BVF map was then directly converted to a hexahedral (brick) FE with dimensions equal to the voxel size. Tissue material properties were assumed to be isotropic and linearly elastic, with each FE's elastic modulus ( $E$ ) set linearly proportional to the respective voxel's BV/TV (BVF) value (Figure 1), such that  $E = (15 \text{ GPa}) \times \text{BVF}$  [29]. Poisson's ratio was assumed to be 0.3 [29]. Simulated compression was applied along each bone's superior-inferior direction to mimic loading conditions at stance. A constant displacement of 1% strain was applied to all vertices of FEs in the proximal face of the FE mesh, while those in the distal face were kept constrained in the vertical direction. A linear system was extracted from the resulting data and stresses at each strain were then computed using a custom designed FE solver [42].

## Nonlinear FE modeling

At larger deformations, bone no longer exhibits linear stress-strain behavior. Instead,  $E$  has nonlinear dependence on tissue element strain ( $\epsilon_{\text{tissue}}$ ) and can be expressed as a power function of the hyperbolic tangent given by  $E(\epsilon_{\text{tissue}}) = ((\text{sech}((50 \times \epsilon_{\text{tissue}} + 0.53)^{1.4}))^{0.6} + 0.05) \times 15 \text{ GPa}$  [20]. From this, a nonlinear system was set up and resultant stresses were calculated using an iterative algorithm as detailed by Zhang et al [20]. Once again, Poisson's ratio was assumed to be 0.3. Stresses were calculated for each applied strain level starting at 0.05% strain and increasing in steps of 0.05% strain up to 3% strain to generate the stress-strain curve. All simulations were performed on a laboratory desktop computer with 32 CPU cores and 128 GB of random-access memory.

## Computation of Parameters

Once the 3D BVF maps were subjected to linear and nonlinear FEA to extract the resultant stresses over a range of strain values, stress-strain curves were computed by fitting a cubic polynomial to the points of applied strains and their corresponding stresses. The linear parameter, whole-bone axial stiffness, was computed as the initial tangent of the simulated stress-strain curve, i.e. as the ratio of the reaction force on the proximal face to the applied strain. Post-yield parameters were also calculated. The yield point, which is the point at which plastic deformation occurs, was found using the 0.2% offset rule [43]. The ultimate point, defined as the point of maximum force, was found at the peak location of the stress-strain curve. From these values, toughness and the modulus of resilience were computed as the integral of the fitted cubic polynomial from zero to the ultimate point and from zero to the yield point, respectively. Since tibia is non-uniform in the axial direction, mean cross-

section area was used for calculating stress. Unlike mechanically tested toughness, FEA-derived toughness does not use the bone's failure point, as there is currently no unique quantitative criterion to determine it from a simulated stress-strain curve. Nevertheless, toughness relates to the energy the bone can sustain before failure, while the modulus of resilience relates to the energy the bone can sustain without permanent damage [21].

### Mechanical testing of cadaver bones

Specimens underwent uniaxial compression tests using a servo-hydraulic material testing machine (Instron 8874, Instron, Norwood, MA) equipped with a 100 kN load cell. The 25 mm distal tibia segments were placed loosely between two parallel steel platens and compressed under displacement control at a rate of 1 mm/min. Tests were terminated after ultimate load was reached. Load-displacement and stress-strain curves were generated, and stiffness, yield strength, ultimate strength, Young's modulus, modulus of resilience, and toughness were subsequently computed using the methods outlined in the approach described for FEA. Since tibia is non-uniform in shape, for calculating stress of each sample, we used the mean cross-section area along the axial direction obtained with the help of micro-CT imaging.

### Statistical Analysis

Correlation coefficients between MRI-derived and experimentally obtained bone yield strength, ultimate strength, stiffness, resilience, and toughness were calculated. Correlation coefficients between each of the post-yield parameters and computational stiffness were also calculated. All statistical analyses were performed using software (JMP Pro 12.1.0; SAS Institute, Cary, NC, USA) and statistical significance was set at  $p < 0.05$ .

## Results

### Comparison of MRI and Experimentally Derived Load Deformation Curves

The FE models derived from *in vivo* high-resolution MR images of the distal metaphysis had an average of  $4 \times 10^5$  (range  $3 \times 10^5 - 7 \times 10^5$ ) FEs, requiring an average of 103 minutes (range 86 – 127 minutes) execution time per nonlinear simulation (60 strain levels), which suggests linear computational complexity (Figure 2). A one-on-one comparison of the simulated and experimental stress-strain curves from a representative patient are displayed in Figure 3. The computer simulated curve drops down more gradually post-ultimate strength than does the experimental curve, which is not surprising, as there is no distinct quantitative criterion for failure point from a simulated stress-strain curve. Mean  $\pm$  SD of parameters determined by direct, mechanical testing experiments and computational modeling are listed in Table 1. Two representative strain maps resulting from the finite element simulation are shown in Figure 4.

### Comparison in the Linear Regime

Computationally and experimentally derived axial stiffness, a parameter calculated from the linear regime of the stress-strain curve, showed a strong positive association ( $R^2 = 0.77$ ,  $p < 0.0001$ ), given by the following equation (Figure 5): Computational Stiffness (kN/mm) =  $2.1 + 0.9 * \text{Experimental Stiffness (kN/mm)}$ . A Bland-Altman analysis showed on average a

1.62 kN/mm overestimation of computationally derived stiffness compared to experimentally derived stiffness ( $p = 0.0012$ ).

### Comparison in the Post-Yield Regime

The association between post-yield experimental and computational measures was weaker than in the linear regime (Figure 6). Analyses revealed a moderate correlation for yield strength ( $R^2 = 0.38$ ,  $p = 0.0082$ ), ultimate strength ( $R^2 = 0.40$ ,  $p = 0.0067$ ), and resilience ( $R^2 = 0.46$ ,  $p = 0.0026$ ), but only a weak, albeit significant, correlation for toughness ( $R^2 = 0.26$ ,  $p = 0.036$ ). Bland-Altman analyses found no significant bias between computational and experimental yield strength, ultimate strength, or toughness, but computational resilience was overestimated by 74.2 kPa on average compared to the experimental data ( $p < 0.0001$ ).

### Association between Stiffness and Post-yield Measures

Computationally derived stiffness was significantly correlated with experimentally derived yield strength ( $R^2 = 0.48$ ,  $p = 0.0022$ ) and ultimate strength ( $R^2 = 0.58$ ,  $p = 0.0004$ ), suggesting the possibility of estimating post-yield strength measures using a computationally less expensive linear simulation (Figure 7). However, the correlations between computationally derived stiffness and experimentally derived resilience ( $R^2 = 0.22$ ,  $p = 0.0603$ ) and toughness ( $R^2 = 0.22$ ,  $p = 0.059$ ) did not reach statistical significance.

## Discussion

The ability to estimate bone's mechanical competence *in vivo* using high-resolution MRI-based FE models has previously been explored. The resulting estimations can be crucial for testing treatment efficacy or monitoring disease progression. Although MRI-derived mechanical parameters of the distal skeletal extremities have been compared with those obtained from high-resolution micro-CT images of cadaveric bone, mechanical bone parameters derived from linear and nonlinear high-resolution MRI-based  $\mu$ FE models have not been directly validated. We sought to do so by subjecting distal tibia specimens to both high-resolution MRI-based FEA and mechanical testing *ex vivo*, using a protocol analogous to that used for *in vivo* imaging.

Both MRI and HR-pQCT have sufficient spatial resolution to allow generation of micro-level FE models of distal skeletal extremities. HR-pQCT based computational models have been shown to identify participants with and without fragility fractures independent of DXA BMD [44, 45]. Furthermore, MRI-based mechanical analysis has proven useful in detecting treatment efficacy and deterioration in bone, even in the absence of any significant change in BMD [28, 29, 46]. Our study provides direct validation for high-resolution imaging based assessment of bone stiffness using linear FEA and nonlinear post-yield FEA at the distal tibia, corroborating the validation reported by McNeil et al. for computational assessment of mechanical competence at the radius using HR-pQCT [37]. Furthermore, our data show that computationally derived distal tibia stiffness is a significant predictor of the experimentally derived post-yield measures of yield strength and ultimate strength. Similarly, McNeil et al. found that experimentally derived ultimate strength of cadaveric human radius samples



obtained from ten donors was highly correlated with computationally derived stiffness ( $R^2 = 0.97$ ). This could potentially enable the use of a linear FE calculation, which is computationally inexpensive compared to nonlinear analysis, to estimate post-yield measures such as yield strength and ultimate strength. However, while our data also showed experimental toughness and resilience to be significantly correlated with their nonlinear FE-derived counterparts, computational stiffness calculated from a linear FE simulation were not significantly correlated with experimental toughness and resilience. This data suggest that linear analysis may not reflect complete post-yield behavior and highlight the usefulness of nonlinear analysis.

Bone fracture is a mechanical phenomenon primarily determined by the ability of bone to withstand various loading conditions. Clinical management of bone diseases is currently largely based on bone density, used as a surrogate for bone strength. Recent advances in high-resolution bone imaging by MRI and HR-pQCT have allowed the microstructure and density of bone to be incorporated in the evaluation of bone health. While microstructural integrity of bone is an important determinant of bone strength, microstructural parameters do not take into account the external loading conditions exerted on bone during a fracture, for instance. High-resolution imaging based micro-FEA, on the other hand, can incorporate certain loading conditions in addition to bone mass and microstructural connectivity to determine the overall bone strength of both trabecular and cortical bone compartments. Our data demonstrate that mechanical parameters derived in this manner at the distal tibia are significantly correlated with experimentally determined values, which supports the use of high-resolution imaging based FE evaluation of bone's mechanical competence in human subjects. It is worth noting that correlations between experimental and computational post-yield parameters were not strong and may not be suitable for predicting absolute strength on their own. Used longitudinally, however, they may be useful for evaluating disease progression or treatment efficacy.

The distal tibia has been the site of choice for high-resolution pQCT or MRI-based translational studies that evaluate the effects of bone disease and therapy on bone microstructure and mechanical competence. While distal tibia fractures are not as common hip, spine, or Colles fractures, the distal tibia has a number of advantages as a surrogate load-bearing site for high-resolution bone imaging. Compared to the central skeleton, the distal tibia requires lower radiation doses to evaluate bone microstructure using HR-pQCT, and requires smaller RF coils for MRI, therefore yielding higher SNR. Furthermore, microstructural and mechanical parameters derived from the distal tibia using high-resolution imaging of human subjects have been shown to correlate significantly with bone health of the hip [47] and spine [48].

MRI is the modality of choice for the comprehensive evaluation of the entire musculoskeletal system, including bone, cartilage, tendons, meniscus, ligaments, and bone marrow. Furthermore, MRI allows for imaging at various resolution regimes and contrast schemes via judicious design of pulse sequences or modifications to the protocols provided by scanner manufacturers. Such flexibility has paved the way for diagnostics and therapy evaluation capabilities far beyond the structural evaluation of bone throughout the skeleton. Additionally, the ubiquity of MRI allows newly developed and validated techniques to reach

a larger patient population. Our study used the FLASE sequence to generate high-resolution images of the distal tibia on a 3-Tesla system from a major MRI manufacturer. Previous MRI studies have demonstrated that microstructural images of bone can be obtained using various pulse sequences [49, 50] at a number of anatomical sites [32, 51–53] using different field strengths [28, 54] with MRI systems from various manufacturers [55].

To ensure accurate representation of bone microstructure in FE models, the imaging resolution used should be at least in the order of trabecular dimensions. For the computational assessment of bone parameters, we utilized a voxel size typically used for translational high-resolution MRI of the distal extremities. Previous work on human cadaveric distal tibia samples has shown that MRI-based mechanical parameters derived using FEA in this resolution regime are highly correlated with those derived from 25  $\mu\text{m}$  voxel size micro-CT images [19]. MRI has the flexibility to image bone microstructure at various resolutions, including 0.05 mm [22] and 0.16 mm [19, 39] isotropic voxel sizes at peripheral skeletal sites and ~0.2 mm voxel size at central sites, such as the proximal femur [32, 56]. Since increased resolution generally requires greater scan time, future studies should investigate the optimum image resolution for ensuring a strong correlation between computationally obtained and mechanically tested bone parameters.

Unlike X-ray based methods, cadaveric bone imaging through MRI is more challenging than in-vivo imaging for several reasons. First, air that leaks into the marrow space during sample preparation creates signal voids and appears as “bone” on MRI. Second, air inclusions cause magnetic susceptibility artifacts causing artificial broadening of trabecular bone thickness. Third, frozen samples produce substantially lower signal-to-noise ratio even after thawing overnight compared to in-vivo imaging. Fourth, image contrast between bone and background (i.e., air) is weak, which subjects image segmentation to error. All these issues combined could explain the overestimation of MRI-derived parameters during cadaveric imaging as seen in Figure 6, similar to previous reports [19].

There are several limitations of this study. First, only axial compression was tested, disregarding fractures due to shearing or tension. However, load-bearing strength under axial compression is correlated with both bending strength and the loading conditions of a fall [57]. Furthermore, this study focused on high-resolution MRI-based mechanical assessment at distal extremities because high-resolution MR imaging of the hip has only recently been explored [33, 56, 58]. Conventional high-resolution MRI is unable to provide information about bone mineral density, unlike CT-based approaches, which could incorporate variations in bone mineral density into finite element models [59, 60]. Another limitation is that our FE model does not directly incorporate the viscoelastic properties of bone and assumes slow loading rate. Furthermore, we compared experimental and MRI-derived mechanical measures only up to the ultimate point. Further algorithmic development is needed to predict the actual fracture point. Additionally, all FE simulations were performed on a high-end computer workstation equipped with 32 CPU cores. Had a computer with fewer cores been utilized, the computation time would have been longer. However, since standard desktop computers are becoming faster with an increasing number of CPU cores, clinical utility of our computational biomechanics framework is expected to improve.



## Conclusion

The present study supports the notion that MRI-based linear and nonlinear FE models have potential for predicting mechanical competence of distal extremities. Our results directly validate the use of these models to monitor bone microstructure changes in individuals suffering from conditions that affect bone mineral homeostasis, as has been done recently in the authors' laboratory [19, 21, 29]. Further validation studies are needed to determine the potential of high-resolution imaging based computational analysis as a viable tool for evaluating bone strength at more common fracture sites, such as the vertebral column or hip. The ability to predict the mechanical competence of human bone could improve the clinical assessment of fracture risk and monitoring response to treatment.

## Acknowledgments

This study was supported by the National Institutes of Health Grants R01 AG 038693, R01 AR 068382, K25 AR060283, and Penn Center for Musculoskeletal Disorders, award number P30AR06919. The content is solely the responsibility of the authors and does not necessarily represent the official views of the National Institutes of Health.

## References

1. Qu X, et al. Association between physical activity and risk of fracture. *J Bone Miner Res.* 2014; 29(1):202–11. [PubMed: 23813682]
2. Kanis JA, et al. The diagnosis of osteoporosis. *J Bone Miner Res.* 1994; 9(8):1137–41. [PubMed: 7976495]
3. Heaney RP. Is the paradigm shifting? *Bone.* 2003; 33(4):457–465. [PubMed: 14555248]
4. Schuit SC, et al. Fracture incidence and association with bone mineral density in elderly men and women: the Rotterdam Study. *Bone.* 2004; 34(1):195–202. [PubMed: 14751578]
5. Stone KL, et al. BMD at multiple sites and risk of fracture of multiple types: Long-term results from the study of osteoporotic fractures. *Journal of Bone and Mineral Research.* 2003; 18(11):1947–1954. [PubMed: 14606506]
6. Siris ES, et al. The effect of age and bone mineral density on the absolute, excess, and relative risk of fracture in postmenopausal women aged 50–99: results from the National Osteoporosis Risk Assessment (NORA). *Osteoporos Int.* 2006; 17(4):565–74. [PubMed: 16392027]
7. Hui SL, Slemenda CW, Johnston CC. Age and Bone Mass as Predictors of Fracture in a Prospective-Study. *Journal of Clinical Investigation.* 1988; 81(6):1804–1809. [PubMed: 3384952]
8. Cummings SR, et al. Appendicular Bone-Density and Age Predict Hip Fracture in Women. *Jama-Journal of the American Medical Association.* 1990; 263(5):665–668.
9. Ott SM, et al. When Bone Mass Fails to Predict Bone Failure. *Calcified Tissue International.* 1993; 53:S7–S13. [PubMed: 8275383]
10. Small RE. Uses and limitations of bone mineral density measurements in the management of osteoporosis. *MedGenMed.* 2005; 7(2):3.
11. Kanis JA, et al. Interpretation and use of FRAX in clinical practice. *Osteoporos Int.* 2011; 22(9): 2395–411. [PubMed: 21779818]
12. Peacock M, et al. Better discrimination of hip fracture using bone density, geometry and architecture. *Osteoporos Int.* 1995; 5(3):167–73. [PubMed: 7655177]
13. Karlsson KM, et al. Femoral neck geometry and radiographic signs of osteoporosis as predictors of hip fracture. *Bone.* 1996; 18(4):327–30. [PubMed: 8726389]
14. MacNeil JA, Boyd SK. Accuracy of high-resolution peripheral quantitative computed tomography for measurement of bone quality. *Med Eng Phys.* 2007; 29(10):1096–105. [PubMed: 17229586]
15. van Rietbergen B. Micro-FE analyses of bone: State of the art. *Noninvasive Assessment of Trabecular Bone Architecture and the Competence of Bone.* 2001; 496:21–30.

16. Kabel J, et al. The role of an effective isotropic tissue modulus in the elastic properties of cancellous bone. *J Biomech.* 1999; 32(7):673–80. [PubMed: 10400354]
17. Ladd AJ, et al. Finite-element modeling of trabecular bone: comparison with mechanical testing and determination of tissue modulus. *J Orthop Res.* 1998; 16(5):622–8. [PubMed: 9820288]
18. Arbenz P, et al. A scalable multi-level preconditioner for matrix-free mu-finite element analysis of human bone structures. *International Journal for Numerical Methods in Engineering.* 2008; 73(7): 927–947.
19. Rajapakse CS, et al. Computational biomechanics of the distal tibia from high-resolution MR and micro-CT images. *Bone.* 2010; 47(3):556–63. [PubMed: 20685323]
20. Zhang N, et al. Potential of in vivo MRI-based nonlinear finite-element analysis for the assessment of trabecular bone post-yield properties. *Med Phys.* 2013; 40(5):052303. [PubMed: 23635290]
21. Zhang N, et al. Assessment of trabecular bone yield and post-yield behavior from high-resolution MRI-based nonlinear finite element analysis at the distal radius of premenopausal and postmenopausal women susceptible to osteoporosis. *Acad Radiol.* 2013; 20(12):1584–91. [PubMed: 24200486]
22. Rajapakse CS, et al. Implications of noise and resolution on mechanical properties of trabecular bone estimated by image-based finite-element analysis. *J Orthop Res.* 2009; 27(10):1263–71. [PubMed: 19338030]
23. Mueller TL, et al. Computational finite element bone mechanics accurately predicts mechanical competence in the human radius of an elderly population. *Bone.* 2011; 48(6):1232–8. [PubMed: 21376150]
24. VanRietbergen B, et al. Direct mechanics assessment of elastic symmetries and properties of trabecular bone architecture. *Journal of Biomechanics.* 1996; 29(12):1653–1657. [PubMed: 8945668]
25. Bevill G, Keaveny TM. Trabecular bone strength predictions using finite element analysis of micro-scale images at limited spatial resolution. *Bone.* 2009; 44(4):579–84. [PubMed: 19135184]
26. MacNeil JA, et al. Preservation of periarticular cancellous morphology and mechanical stiffness in post-traumatic experimental osteoarthritis by antiresorptive therapy. *Clin Biomech (Bristol, Avon).* 2008; 23(3):365–71.
27. Zhang XH, et al. In vivo microMRI-based finite element and morphological analyses of tibial trabecular bone in eugonadal and hypogonadal men before and after testosterone treatment. *J Bone Miner Res.* 2008; 23(9):1426–34. [PubMed: 18410234]
28. Wehrli FW, et al. Mechanical implications of estrogen supplementation in early postmenopausal women. *J Bone Miner Res.* 2010; 25(6):1406–14. [PubMed: 20200948]
29. Rajapakse CS, et al. Micro-MR imaging-based computational biomechanics demonstrates reduction in cortical and trabecular bone strength after renal transplantation. *Radiology.* 2012; 262(3):912–20. [PubMed: 22357891]
30. Majumdar S. Magnetic resonance imaging of trabecular bone structure. *Top Magn Reson Imaging.* 2002; 13(5):323–34. [PubMed: 12464745]
31. Wehrli FW. Structural and functional assessment of trabecular and cortical bone by micro magnetic resonance imaging. *J Magn Reson Imaging.* 2007; 25(2):390–409. [PubMed: 17260403]
32. Chang G, et al. Feasibility of three-dimensional MRI of proximal femur microarchitecture at 3 tesla using 26 receive elements without and with parallel imaging. *J Magn Reson Imaging.* 2014; 40(1):229–38. [PubMed: 24711013]
33. Han M, et al. Variable flip angle three-dimensional fast spin-echo sequence combined with outer volume suppression for imaging trabecular bone structure of the proximal femur. *J Magn Reson Imaging.* 2015; 41(5):1300–10. [PubMed: 24956149]
34. Li X, et al. Quantification of vertebral bone marrow fat content using 3 Tesla MR spectroscopy: reproducibility, vertebral variation, and applications in osteoporosis. *J Magn Reson Imaging.* 2011; 33(4):974–9. [PubMed: 21448966]
35. Mostoufi-Moab S, et al. Adverse Fat Depots and Marrow Adiposity Are Associated With Skeletal Deficits and Insulin Resistance in Long-Term Survivors of Pediatric Hematopoietic Stem Cell Transplantation. *J Bone Miner Res.* 2015; 30(9):1657–66. [PubMed: 25801428]

36. Liu XS, et al. Accuracy of high-resolution in vivo micro magnetic resonance imaging for measurements of microstructural and mechanical properties of human distal tibial bone. *J Bone Miner Res.* 2010; 25(9):2039–50. [PubMed: 20499379]
37. Macneil JA, Boyd SK. Bone strength at the distal radius can be estimated from high-resolution peripheral quantitative computed tomography and the finite element method. *Bone.* 2008; 42(6): 1203–13. [PubMed: 18358799]
38. Wald MJ, et al. Predicting trabecular bone elastic properties from measures of bone volume fraction and fabric on the basis of micromagnetic resonance images. *Magn Reson Med.* 2012; 68(2):463–73. [PubMed: 22162036]
39. Wald MJ, et al. Structural and mechanical parameters of trabecular bone estimated from in vivo high-resolution magnetic resonance images at 3 tesla field strength. *J Magn Reson Imaging.* 2010; 31(5):1157–68. [PubMed: 20432352]
40. Magland JF, Wald MJ, Wehrli FW. Spin-echo micro-MRI of trabecular bone using improved 3D fast large-angle spin-echo (FLASE). *Magn Reson Med.* 2009; 61(5):1114–21. [PubMed: 19215044]
41. Vasilic B, Wehrli FW. A novel local thresholding algorithm for trabecular bone volume fraction mapping in the limited spatial resolution regime of in vivo MRI. *Ieee Transactions on Medical Imaging.* 2005; 24(12):1574–1585. [PubMed: 16353372]
42. Magland JF, et al. Computationally-optimized bone mechanical modeling from high-resolution structural images. *PLoS One.* 2012; 7(4):e35525. [PubMed: 22558164]
43. Niebur GL, et al. High-resolution finite element models with tissue strength asymmetry accurately predict failure of trabecular bone. *J Biomech.* 2000; 33(12):1575–83. [PubMed: 11006381]
44. Boutroy S, et al. Finite element analysis based on in vivo HR-pQCT images of the distal radius is associated with wrist fracture in postmenopausal women. *J Bone Miner Res.* 2008; 23(3):392–9. [PubMed: 17997712]
45. Vilayphiou N, et al. Finite element analysis performed on radius and tibia HR-pQCT images and fragility fractures at all sites in men. *J Bone Miner Res.* 2011; 26(5):965–73. [PubMed: 21541999]
46. Al Mukaddam M, et al. Effects of testosterone and growth hormone on the structural and mechanical properties of bone by micro-MRI in the distal tibia of men with hypopituitarism. *J Clin Endocrinol Metab.* 2014; 99(4):1236–44. [PubMed: 24423356]
47. Liu XS, et al. Bone density, geometry, microstructure, and stiffness: Relationships between peripheral and central skeletal sites assessed by DXA, HR-pQCT, and cQCT in premenopausal women. *J Bone Miner Res.* 2010; 25(10):2229–38. [PubMed: 20499344]
48. Rajapakse CS, et al. Vertebral deformities and fractures are associated with MRI and pQCT measures obtained at the distal tibia and radius of postmenopausal women. *Osteoporos Int.* 2014; 25(3):973–82. [PubMed: 24221453]
49. Krug R, et al. Fully balanced steady-state 3D-spin-echo (bSSSE) imaging at 3 Tesla. *Magn Reson Med.* 2006; 56(5):1033–40. [PubMed: 16986110]
50. Magland JF, et al. 3D fast spin echo with out-of-slab cancellation: a technique for high-resolution structural imaging of trabecular bone at 7 Tesla. *Magn Reson Med.* 2010; 63(3):719–27. [PubMed: 20187181]
51. Chang G, et al. In vivo estimation of bone stiffness at the distal femur and proximal tibia using ultra-high-field 7-Tesla magnetic resonance imaging and micro-finite element analysis. *J Bone Miner Metab.* 2012; 30(2):243–51. [PubMed: 22124539]
52. Lam SC, et al. Performance of the MRI-based virtual bone biopsy in the distal radius: serial reproducibility and reliability of structural and mechanical parameters in women representative of osteoporosis study populations. *Bone.* 2011; 49(4):895–903. [PubMed: 21784189]
53. Guglielmi G, et al. Magnetic resonance imaging of the calcaneus: preliminary assessment of trabecular bone-dependent regional variations in marrow relaxation time compared with dual X-ray absorptiometry. *Acad Radiol.* 1996; 3(4):336–43. [PubMed: 8796684]
54. Krug R, et al. In vivo ultra-high-field magnetic resonance imaging of trabecular bone microarchitecture at 7 T. *J Magn Reson Imaging.* 2008; 27(4):854–9. [PubMed: 18383263]

55. Banerjee S, et al. Application of refocused steady-state free-precession methods at 1.5 and 3 T to in vivo high-resolution MRI of trabecular bone: simulations and experiments. *J Magn Reson Imaging*. 2005; 21(6):818–25. [PubMed: 15906346]
56. Chang G, et al. Finite element analysis applied to 3-T MR imaging of proximal femur microarchitecture: lower bone strength in patients with fragility fractures compared with control subjects. *Radiology*. 2014; 272(2):464–74. [PubMed: 24689884]
57. Lochmuller EM, et al. Radius bone strength in bending, compression, and falling and its correlation with clinical densitometry at multiple sites. *J Bone Miner Res*. 2002; 17(9):1629–38. [PubMed: 12211433]
58. Krug R, et al. Feasibility of in vivo structural analysis of high-resolution magnetic resonance images of the proximal femur. *Osteoporos Int*. 2005; 16(11):1307–14. [PubMed: 15999292]
59. Bourne BC, van der Meulen MC. Finite element models predict cancellous apparent modulus when tissue modulus is scaled from specimen CT-attenuation. *J Biomech*. 2004; 37(5):613–21. [PubMed: 15046990]
60. Jaasma MJ, et al. Biomechanical effects of intraspecimen variations in tissue modulus for trabecular bone. *J Biomech*. 2002; 35(2):237–46. [PubMed: 11784542]

**Highlights**

- MRI-based finite element models effectively assess mechanical parameters of distal skeletal extremities.
- Computationally and experimentally obtained values of stiffness, yield strength, ultimate strength, resilience, and toughness were correlated.
- Experimentally derived yield strength and ultimate strength correlated with MRI-derived stiffness, suggesting feasibility of estimating strength measures using computationally less expensive linear simulations.

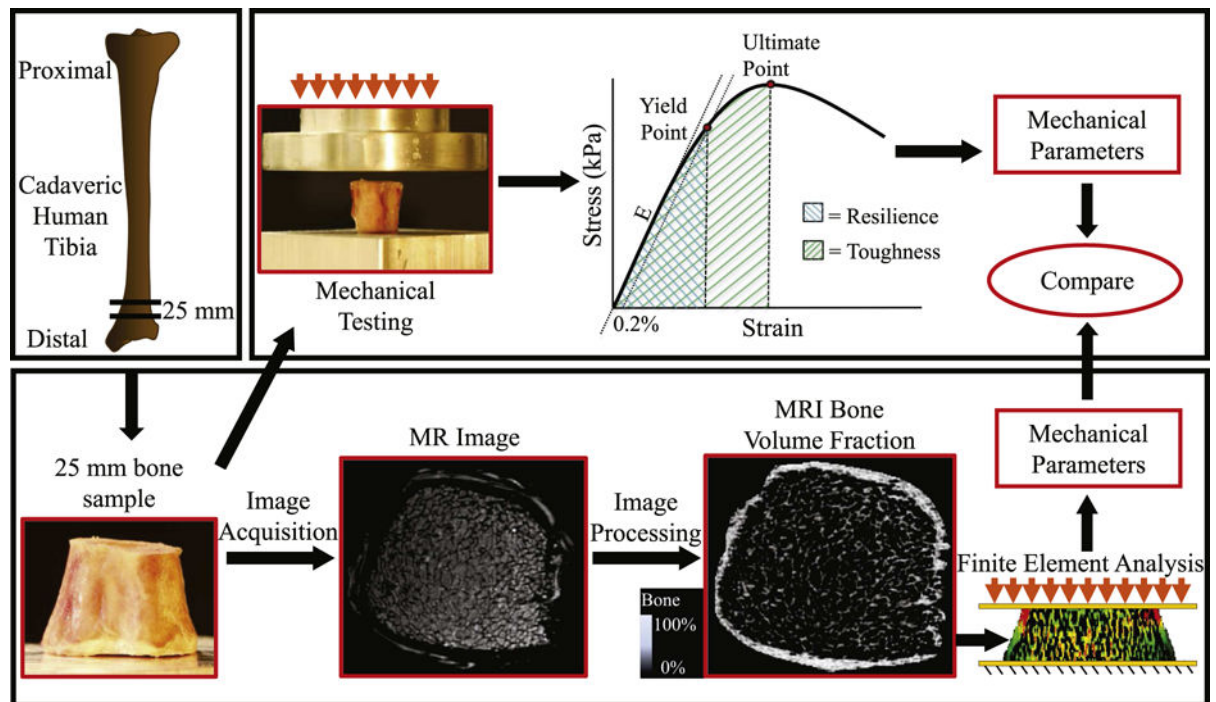


**Figure 1.** Schematic flowchart illustrating the *ex vivo* validation of MRI-based assessment of bone stiffness, resilience, and toughness, including specimen preparation, MR imaging and processing, finite element modeling, and mechanical testing. E = Young's Modulus.



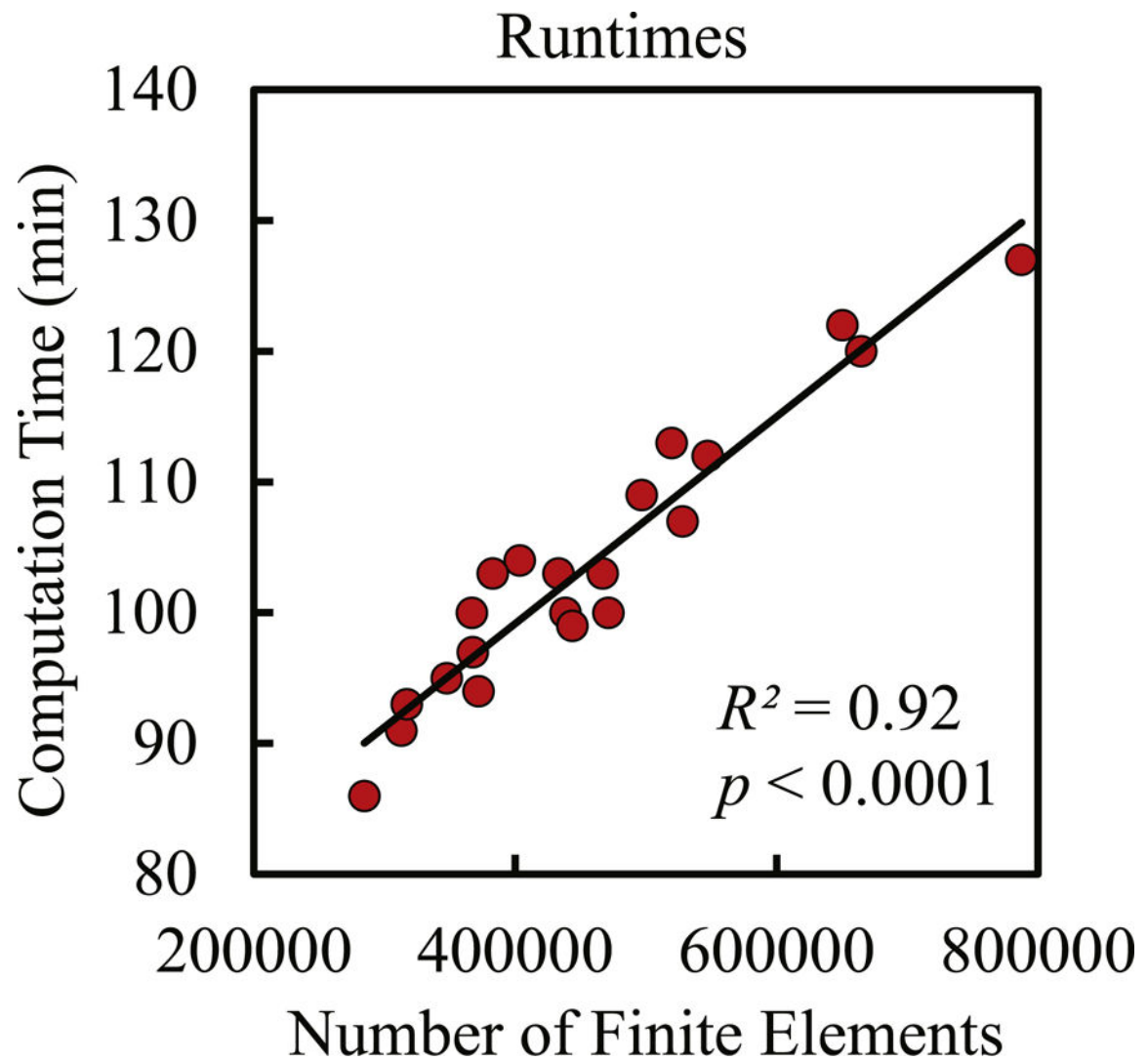


**Figure 2.** Association between number of finite elements and wall clock computation time for nonlinear simulations.

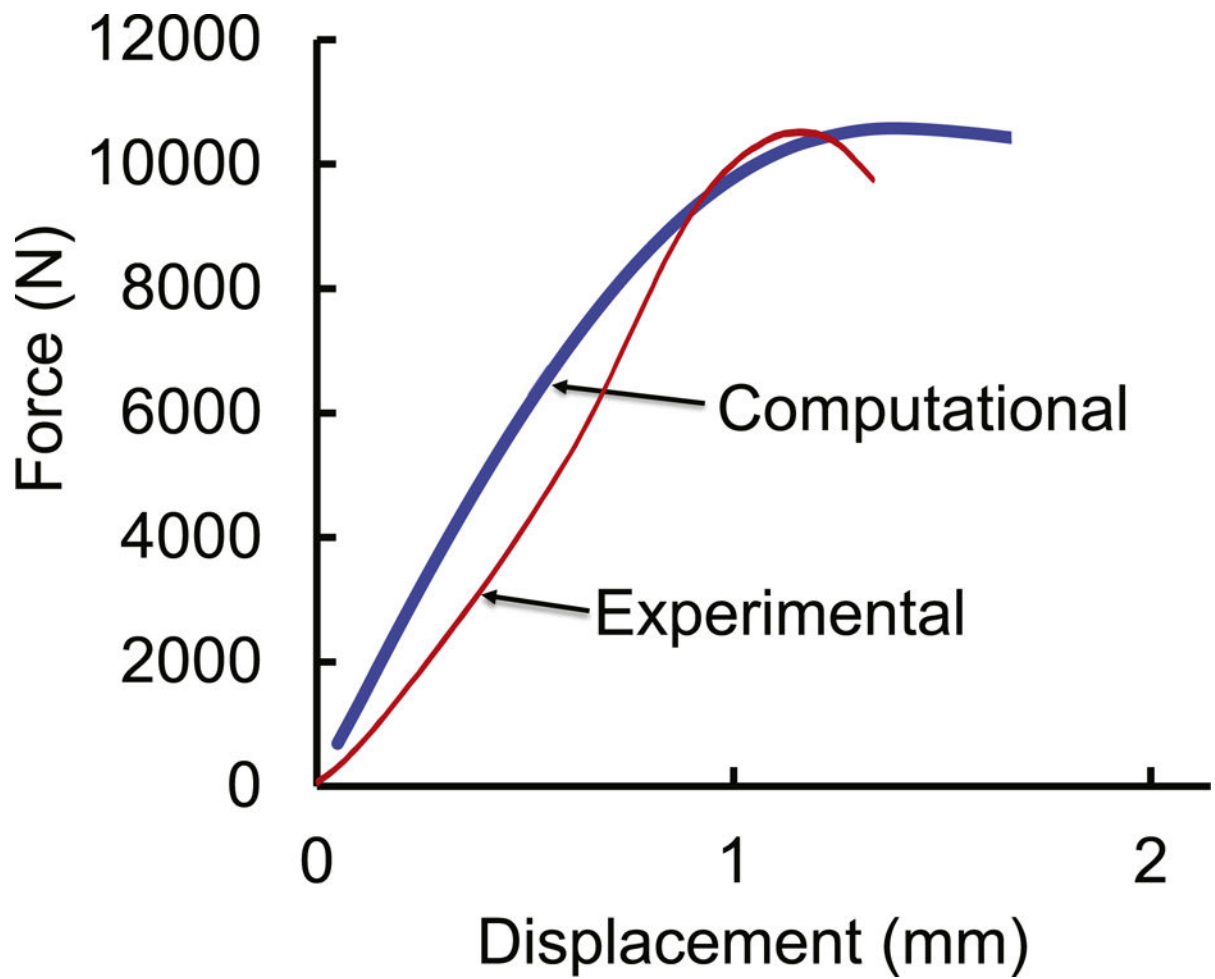


**Figure 3.**  
Comparison of experimentally and computationally derived load-deformation curves for a representative distal tibia specimen.

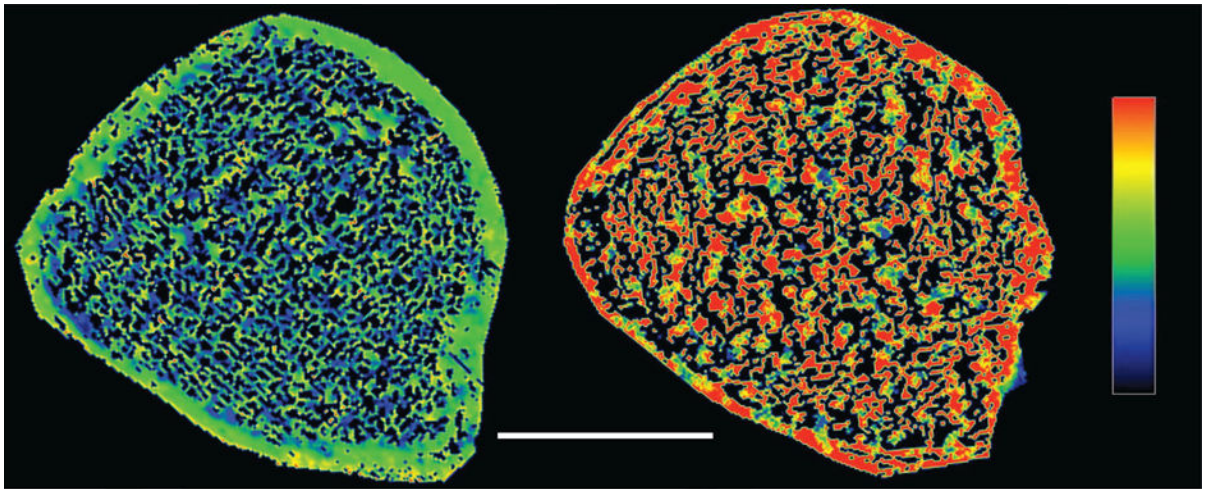


**Figure 4.** Computationally derived representative mid-section strain distribution of a tibia specimen that had (A) high ultimate strength (13 kN), thicker compact cortical bone, and well connected trabecular network and (B) low ultimate strength (3 kN), thinner porous cortical bone, and disorganized trabecular network.

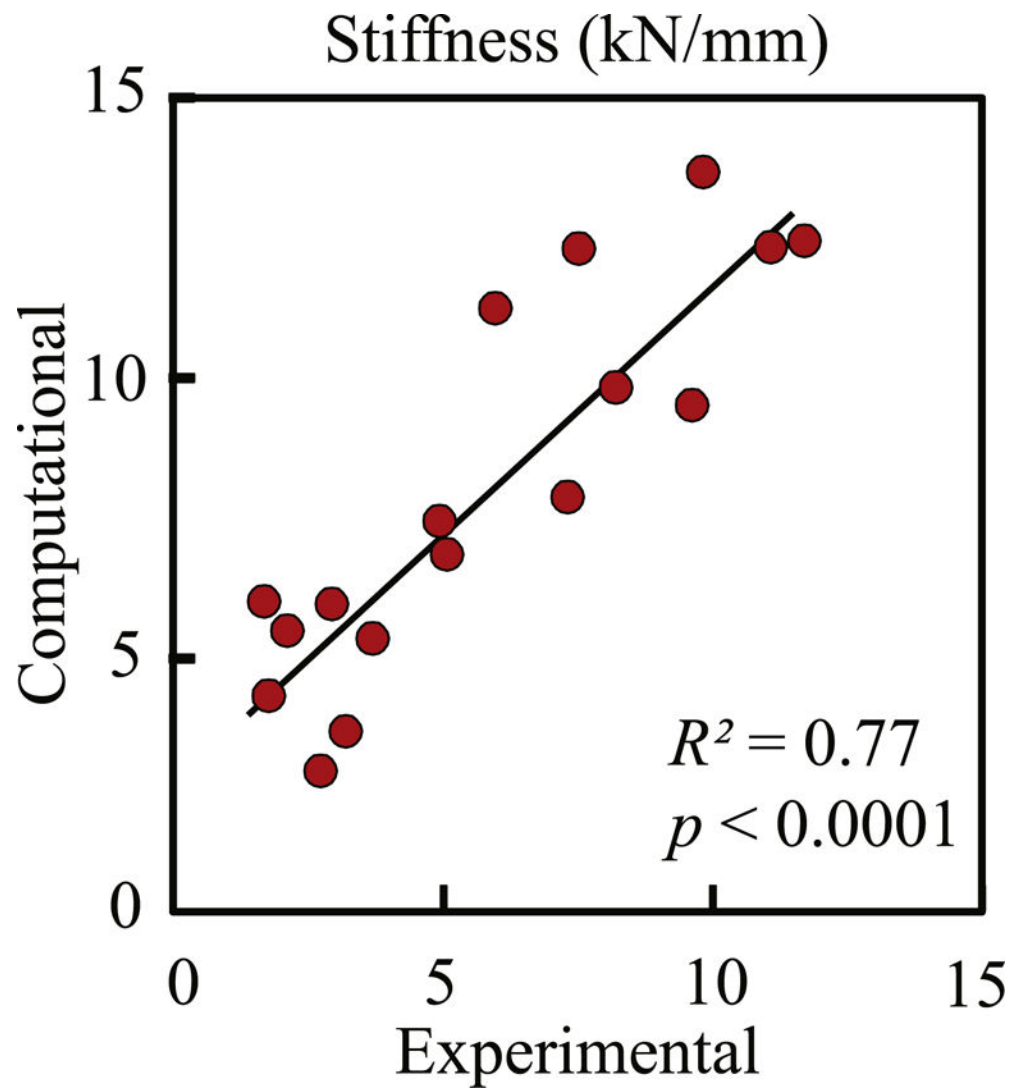


**Figure 5.** Correlation plot illustrating the stiffness values for each bone specimen as estimated from MRI images (computational) and from mechanical testing (experimental).

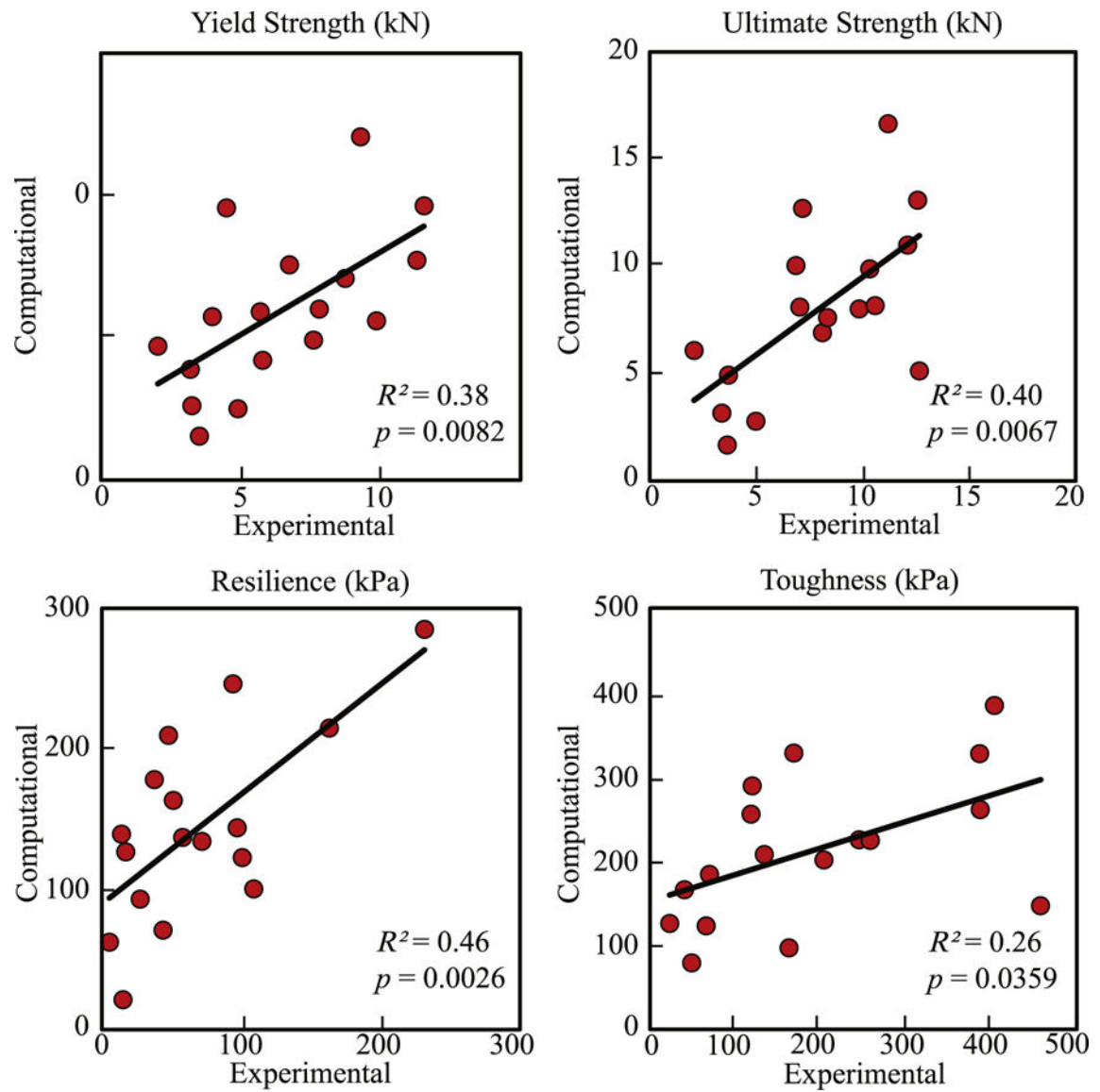


**Figure 6.** Correlation plots illustrating the yield strength (kN), ultimate strength (kN), resilience (kPa), and toughness (kPa) for each bone specimen as estimated computationally from MRI images and experimentally from mechanical testing.

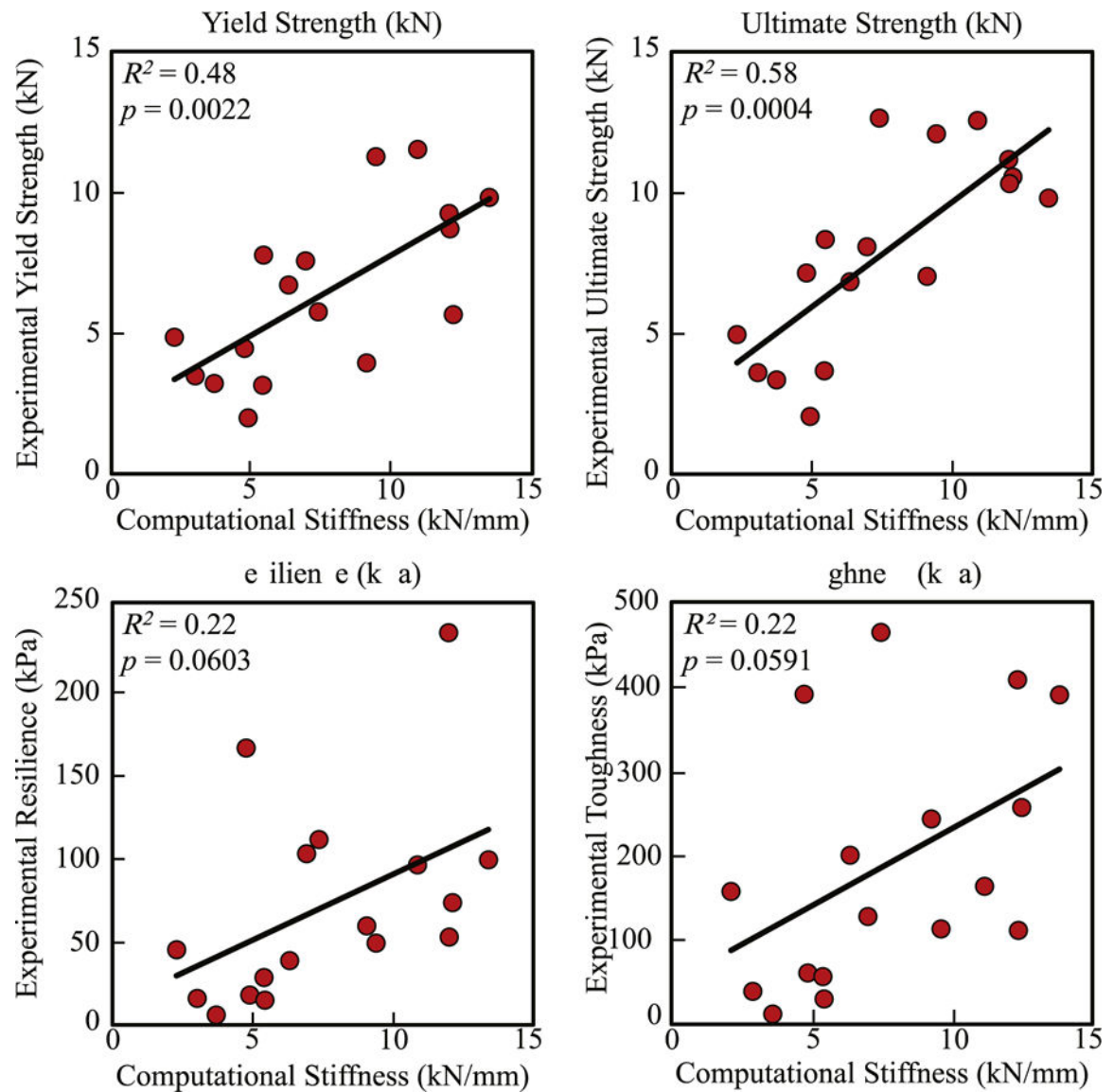


**Figure 7.**

Correlation plots illustrating the experimental post-yield parameters of yield strength (kN), ultimate strength (kN), resilience (kPa), and toughness (kPa) for each bone specimen versus computational stiffness (kN/mm) derived from linear finite element analysis.



**Table 1**

Mean  $\pm$  SD of parameters determined by direct mechanical testing experiments and computational modeling.

Parameter	Experimental	Computational	<i>p</i>
Stiffness (kN/mm)	6.00 $\pm$ 3.37	7.57 $\pm$ 3.44	0.0012
Yield Strength (kN)	6.44 $\pm$ 2.93	5.85 $\pm$ 2.71	0.40
Ultimate Strength (kN)	7.91 $\pm$ 3.46	7.95 $\pm$ 3.86	0.92
Resilience (kPa)	70.1 $\pm$ 59.2	143 $\pm$ 66	<0.0001
Toughness (kPa)	193 $\pm$ 140	222 $\pm$ 94	0.52